# Destabilization of a flat nematic-isotropic interface

John Bechhoefer,* Adam J. Simon, and Albert Libchaber

*The James Franck Institute and The Enrico Fermi Institute, The University of Chicago, 5640 South Ellis Avenue, Chicago, Illinois 60637*

Patrick Oswald

*Laboratoire de Physique de l'Ecole Normale Supérieure de Lyon, 46 Allée d'Italie, 69364 Lyon CEDEX 07, France*

(Received 16 January 1989)

We present experiments on the directional solidification of a moving nematic-isotropic interface. We study the bifurcation and marginal stability of the interface in a system of 4,4'-*n*-octylcyanobiphenyl (8CB) with the impurity hexachloroethane $C_2Cl_6$ added. In the velocity, temperature-gradient parameter space, we can trace the marginal stability line, in qualitative agreement with theory. A quantitative analysis shows that three-dimensional effects, such as solute-driven convection and the thickness of the sample, must be considered.

## I. INTRODUCTION

In this paper we study the directional solidification of a liquid crystal, in particular the marginal stability of a nematic-isotropic interface as it is dragged along at a fixed, controllable velocity by a moving temperature gradient, also controllable. In previous work,[1] we reported observations on pattern formation in such a system and suggested[2] that the impurity-diffusion version of the Mullins-Sekerka instability[3] was responsible. Armitage and Price[4] had earlier observed the Mullins-Sekerka instability in undercooled melts of the liquid crystal *p*-azoxyanisole (PAA). Their qualitative analysis neglected the impurity effects which are dominant.

A primary purpose of the present work is to examine whether the observed pattern formation is due to the Mullins-Sekerka instability. In Sec. II we summarize the Mullins-Sekerka theory of the linear stability of a flat interface, as it applies to our experiment.

In Sec. III we describe the experiment itself. In brief, as shown in Fig. 1, a (nearly) two-dimensional sample is placed into a temperature gradient that points in the plane of the sample. The temperature gradient is set by putting a thin sandwich of glass filled with chemical across a gap between two ovens. The temperatures of the two ovens are chosen so that there is a phase transition in between the ovens, giving rise to a straight interface. The sample is set into motion at a velocity $v$; after a transient, the interface freezes at $-v$ in order to stay at the same temperature. At low velocities, the interface remains a straight line; at high velocities, the interface destabilizes into a wavy pattern, the understanding of which is our primary goal. The experiment may be set up in such a way that the interface pattern formation is the result of adding impurities to the sample. The interface remains a straight line in the absence of impurities for the range of velocities and temperature gradients accessible in our experiment.

Figure 2 shows steady interface profiles as a function of velocity. As we have remarked in earlier work,[1,2] the bifurcation from the flat interface in Fig. 2(a) to the slightly deformed interface in Fig. 2(b) is supercritical. In this paper we shall be concerned only with the quantitative analysis of the loss of stability of a flat interface. The reader should note, though, that the nonlinear behavior of the interface is rich and barely explored.[5,6]

In Sec. IV we present our primary experimental results, namely, the determination of the marginal stability curve in the space of velocity and imposed temperature gradient. The main features of the stability curve are in qualitative agreement with theory. Further, we observe solute-driven convection on the isotropic side of the interface and present a quantitative analysis suggesting that this physical process, ignored in previous theoretical treatments, must be considered.

Finally in Sec. V we discuss in detail the results and try to propose possible explanations for the discrepancy between the physical parameters of 4,4'-*n*-octylcyanobiphenyl (8 CB) and the onset values of velocity and wavelength. Also, the thickness dependence of samples is investigated further.
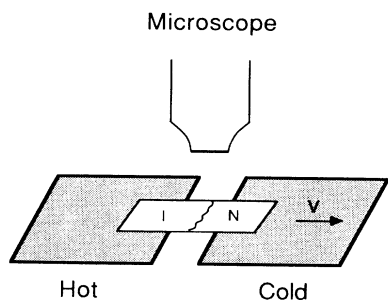


FIG. 1. Basic experimental setup. A thin sample is drawn across two ovens separated by a small gap. Because the temperature field is stationary in the laboratory frame, the interface may be observed via a fixed microscope, as indicated.
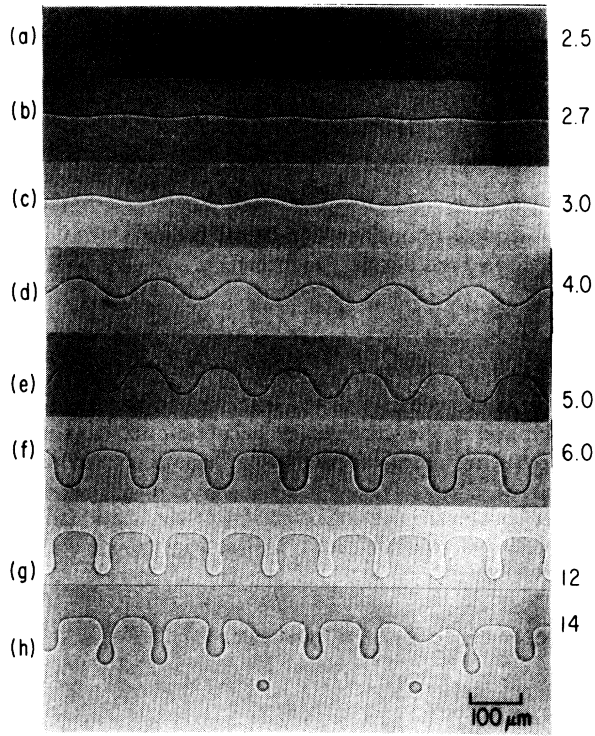
FIG. 2. Interface patterns as the velocity is increased. The numbers to the right of each pattern give the velocity, in $\mu$m/sec. $G = 43\,°C/cm$, $c_0 = 3.0$ mol %, $d = 28\ \mu$m. Phase contrast illumination.

## II. THEORETICAL BACKGROUND

The "standard model" of directional solidification follows a macroscopic thermodynamic approach in which the interface is a surface of zero width separating the phases. Every point is assumed to be in local thermodynamic equilibrium; kinetic processes at the interface are neglected. While such an approximation is valid for low interface velocities, nonequilibrium effects begin to be important for interface velocities of the order of meters per second in solid-liquid systems.[7-10] For liquid crystals, it is possible that such effects enter at lower velocities.

We further assume that the temperature field is imposed by the experimenter, and, in particular, that the release of latent heat may be ignored. See below, Sec. III C. Finally, we begin by assuming that a two-dimensional description is sufficient. In previous work on solid-liquid systems, de Cheveigné et al.[11] established that a meniscus in the vertical plane could have a large effect on the quantitative predictions of the Mullins-Sekerka theory. Subsequent calculations by Caroli et al.[12] have qualitatively confirmed these ideas. In the experimental case, we will clearly have to worry about three-dimensional effects. See Sec. IV, below.

With these assumptions, the field of impurity concentration obeys a diffusion equation in each phase:

$$\frac{\partial c_{N,I}}{\partial t} = D_{N,I}\nabla^2 c_{N,I} \ . \tag{1}$$

The subscript $(N)$ refers to the nematic phase and the $(I)$ refers to the isotropic phase. In the reference frame moving along with the interface, the diffusion equation can be written

$$\frac{\partial c_{N,I}}{\partial t} = D_{N,I}\nabla^2 c_{N,I} + v\frac{\partial c_{N,I}}{\partial y} \ , \tag{2}$$

where $v$ is the average interface velocity. At $y = \pm\infty$, the concentration is $c_0$. The moving coordinate system is illustrated in Fig. 3. Ordinarily, the specification of our problem would be given by a boundary condition for $c$ at some known location. Here, the boundary is unknown, but we specify both $c$ and $\nabla c$ at this unknown boundary.

The equation for $c$ requires consideration of several points of thermodynamics. The first is that impurities alter the melting temperature of a material. By considering the change in chemical potential due to the addition of impurities, one can derive the van 't Hoff law:[13]

$$T_m = T_{N\text{-}I} - \frac{RT_{N\text{-}I}^2}{L}(c_I - c_N) \ . \tag{3}$$

Here, $T_m$ is the phase transition temperature in the impure material, $T_{N\text{-}I}$ is the nematic-isotropic transition in a pure material, $R$ is the ideal gas constant, $L$ is the molar latent heat of the pure nematic-isotropic transition, and $c_I$ and $c_N$ are the concentrations of impurities in the isotropic and nematic phases and are here evaluated at the interface. By equating the chemical potential of the impurity, one can also show that

$$k \equiv \frac{c_N}{c_I} = e^{-\Delta\psi(P,T)/RT_{N\text{-}I}} \ , \tag{4}$$

where we have defined the equilibrium partition coefficient $k$ and where $\Delta\psi(P,T)$ is proportional to the free-energy difference of the impurities between the phases. Note that at a second-order transition, $k = 1$ as all thermodynamic quantities must be continuous.

The phase diagram corresponding to Eqs. (3) and (4) is shown in Fig. 4(b). The liquidus line setting off the iso-
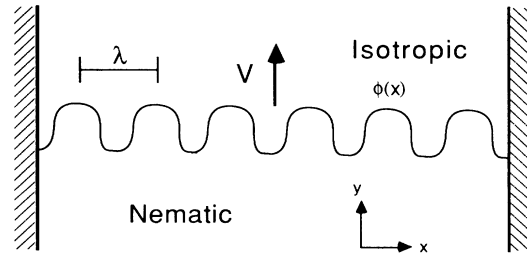


FIG. 3. Coordinate system for directional solidification. The interface pattern has wavelength $\lambda$ and is described by the function $\phi(x)$. The $z$ axis, not shown, is perpendicular to the plane of the figure. The figure shows an aspect ratio (width/$\lambda$) of 6. Actual samples have aspect ratios of $10^2$ to $10^3$.

**(a)**

Concentration

$C_0/k$

$\Delta C$

$C_0$

$l_D$

$v \longrightarrow$

Position

**(b)**

Temperature / Position

$T_m$

(i)

(ii)

(iii)

Isotropic

Nematic

Liquidus

Solidus

$\Delta C$

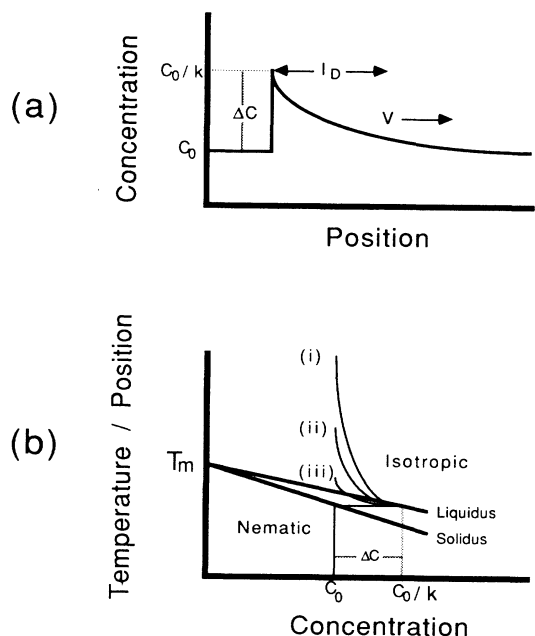$C_0$     $C_0/k$

Concentration

FIG. 4. Concentration profiles for a moving planar interface. (a) Concentration as a function of position. (b) The concentration profile superposed on the impurity-phase diagram. Since the temperature gradient is linear, the $y$ axis is both temperature and position. Curve (i) has $v < v_c$; curve (ii) has $v = v_c$; curve (iii), which dips into the coexistence region, has $v > v_c$.

tropic phase from the coexistence region has a slope whose absolute value is $m = RT_{N\text{-}I}^2(1-k)/L$. The solidus line separating the low-temperature nematic phase from the coexistence region has a slope of absolute value $m/k$. In addition to illustrating a jump in concentration across an isothermal interface, Fig. 4(b) shows that an impure material will have a melting range. Between liquidus and solidus lines, the two phases will coexist in equilibrium. Note that any material will satisfy Eq. (3) at low-enough concentrations. The only question is how low.

The second point of thermodynamics is that surface tension and impurity effects alter the melting temperature of curved interfaces. The Gibbs-Thomson law[13] relates a shift in melting temperature to the curvature $\kappa$ of the interface:

$$T = T_{N\text{-}I}(1 - d_0\kappa) , \qquad (5)$$

$$d_0 = \gamma M_w / L\rho_N . \qquad (6)$$

Here, $d_0$ is the thermal capillary length, $\gamma$ is the surface tension, $M_w$ is the molecular weight of the liquid crystal, and $\rho_N$ is the density of the nematic phase at $T_{N\text{-}I}$.

To get the boundary condition for $c$, we recall that the sample is subjected to a uniform temperature gradient $G$, hence

$$T(y) = T_0 + Gy . \qquad (7)$$

The constant $T_0$ can be adjusted so that $y = 0$ corresponds to the position of the flat interface at $v = 0$. Putting together all our thermodynamic relationships, we have

$$\frac{1}{k}c_N(x,\phi) = c_I(x,\phi) = c_0 \left[ 1 - \frac{Gy}{mc_0} - d_0\frac{T_{N\text{-}I}}{mc_0}\kappa \right] . \qquad (8)$$

The second boundary condition requires that impurities be conserved across the interface:

$$(\hat{n}\cdot\mathbf{v})c_I(x,\phi)(1-k)$$
$$= D_N\hat{n}\cdot\nabla c_N(x,\phi) - D_I\hat{n}\cdot\nabla c_I(x,\phi) , \qquad (9)$$

where $\mathbf{v}$ is the velocity of the interface in the frame of the sample, and $\hat{n}$ is a unit vector perpendicular to the interface, pointing from the nematic phase into the isotropic phase.

This completes the specification of the standard model of directional solidification. Collecting the various equations, we have

$$D_N\nabla^2 c_N + v\frac{\partial c_N}{\partial y} = \frac{\partial c_N}{\partial t}, \quad y < \phi(x)$$

$$D_I\nabla^2 c_I + v\frac{\partial c_I}{\partial y} = \frac{\partial c_I}{\partial t}, \quad y > \phi(x)$$

$$\lim_{y\to-\infty} c_N(x,y) = \lim_{y\to+\infty} c_I(x,y) = c_0 ,$$

$$\frac{c_N(x,\phi)}{k} = c_I(x,\phi) = c_0 \left[ 1 - \frac{Gy}{mc_0} - d_0\frac{T_{N\text{-}I}}{mc_0}\kappa \right] , \qquad (10)$$

$$\kappa(x) = \frac{-\phi''(x)}{[1+\phi'^2(x)]^{3/2}} ,$$

$$(\hat{n}\cdot\mathbf{v})c_I(x,\phi)(1-k)$$
$$= D_N\hat{n}\cdot\nabla c_N(x,\phi) - D_I\hat{n}\cdot\nabla c_I(x,\phi) .$$

In these equations, $\phi(x)$ is the position of the interface and $\kappa(x)$ is the interface curvature.

The standard model considers three physical effects: the diffusion of impurities, the depression of the interface temperature due to impurities, and the change of interface temperature due to curvature. With the imposed temperature gradient there are three length scales for diffusion, thermal, and capillary lengths, respectively,

$$l_D \equiv \frac{D_I}{v} ,$$

$$l_T \equiv \frac{\Delta T}{G} , \qquad (11)$$

$$l_C \equiv d_0 \frac{T_{N\text{-}I}}{\Delta T} .$$

Here, $\Delta T \equiv m\,\Delta c \equiv mc_0(1-k)/k$ represents the temperature difference between liquidus and solidus lines on the equilibrium phase diagram, for a concentration $c_0$, and $\Delta c \equiv c_0(1-k)/k$ is the difference in concentration between the liquidus and solidus lines on the phase diagram [see Fig. 4(b)]. Each length scale has a clear physical meaning. $l_D$ is the length over which the concentration

field falls to $1/e$ of its original value in front of a moving flat interface. $l_T$ is the length over which one moves from the liquidus to the solidus line on the temperature-concentration phase diagram. (On the diagram, this is a temperature, which is converted to a length via $G$.) $l_C$ will be interpreted below as the smallest length scale of interfacial pattern one can observe. For the moment, we note that it is the length that appears when we ask what concentration difference will balance the chemical potential jump across a curved interface. The factor $T_{N-I}/\Delta T$ in $l_C$ accounts for the adjusted surface tension due to the shift in melting temperature due to impurities.

Because there are three length scales in the problem, there are obviously several ways to define the two dimensionless control parameters. In this paper we will adopt the following convention: we shall scale position variables by $l_C$ and define the control parameters $l_C/l_D$ and $l_C/l_T$. This convention has several advantages in comparing theory with experiment.[14] The capillary length $l_C$ is an intrinsic scale of the system, whereas the other two scales are imposed by the experimenter. $l_C$ will turn out to be the smallest length scale of a pattern observable for a given material. The control parameters as defined above are easily interpreted as the dimensionless velocity and temperature gradient, respectively. They can be varied independently by the experimenter. Explicitly, we rescale $x,y,\phi,\kappa$ by $l_C$, $t$ by $l_C^2/D_I$, $c_N$ and $c_I$ by $c_0$, and define $\eta \equiv D_N/D_I$. After rescaling one gets the equation

$$\eta \nabla^2 c_N + v \frac{\partial c_N}{\partial y} = \frac{\partial c_N}{\partial t} ,$$

$$\nabla^2 c_I + v \frac{\partial c_I}{\partial y} = \frac{\partial c_I}{\partial t} ,$$

$$\lim_{y \to -\infty} c_N(x,y) = \lim_{y \to +\infty} c_I(x,y) = 1 , \tag{12}$$

$$\frac{c_N(x,\phi)}{k} = c_I(x,\phi) = 1 - \frac{1-k}{k}(Gy + \kappa) ,$$

$$(\hat{\mathbf{n}} \cdot \mathbf{v}) c_I(x,\phi)(1-k) = \eta \hat{\mathbf{n}} \cdot [\nabla c_N(x,\phi)] - \hat{\mathbf{n}} \cdot [\nabla c_I(x,\phi)] .$$

### A. Zeroth-order solution

The zeroth-order solution to Eq. (12) is a flat interface:

$$\phi_0 = -G^{-1} , \quad c_N(x,y) = 1 ,$$

$$c_I(x,y) = 1 + \left[ \frac{1-k}{k} \right] e^{-v(y - \phi_0)} \tag{13}$$

[see Fig. 4(a)]. Across the interface, the concentration jumps from $c_N = 1$ to $c_I = 1/k$. This "spike" of impurities then decays over a length $1/v$. The faster the interface moves, the steeper is the decay of impurities in front of the interface. In 1953, Tiller et al. proposed that the interfacial instability was the result of "constitutional supercooling."[15] Drawing the solution on a phase diagram [Fig. 4(b)], we see that for large enough $v$, the interface dips into the region of coexistence. It is easy to show that the condition for dipping into the coexistence region

is just $v = G$ (in our dimensionless units). This is called the constitutional-supercooling criterion.

### B. Linear stability analysis

For $v$ and $G \to 0$, the physically appealing picture of constitutional supercooling is accurate. But for larger $v$ and $G$, the surface tension of the interface becomes important and the relation $v = G$ must be modified. A proper linear stability analysis of a moving flat interface was first performed by Mullins and Sekerka.[16,17] We let

$$\phi = -G^{-1} + A(t)\cos(qx) ,$$

$$c_N(t) = 1 + B(t)\cos(qx)e^{-\tilde{Q}[y - \phi(t)]} , \tag{14}$$

$$c_I(t) = 1 + \left[ \frac{1-k}{k} \right] e^{-v[y - \phi(t)]}$$

$$+ D(t)\cos(qx)e^{-Q[y - \phi(t)]} ,$$

where $A(t)$, $B(t)$, and $D(t)$ are small compared to 1 and where $Q$ and $\tilde{Q}$ are to be determined. Inserting these expressions into Eqs. (12), and we get

$$\omega(q;v,G) = \frac{\dot{A}}{A} = -kv^2 + vQ + [vk(1-k) - (Q + \eta k \tilde{Q})]$$

$$\times (G + q^2) , \tag{15}$$

with

$$Q = \frac{v}{2}[1 + (1 + 4q^2/v^2 + 4\omega/v^2)^{1/2}] ,$$

$$\tilde{Q} = \frac{v}{2\eta}[-1 + (1 + 4q^2\eta^2/v^2 + 4\eta^2\omega/v^2)^{1/2}] . \tag{16}$$

At the onset of instability, $\omega = \partial\omega/\partial q = \partial\omega/\partial(q^2) = 0$ gives the bifurcation curve, $G(v)$, separating the region of parameter space where planar fronts are stable from the region where planar fronts are unstable solutions to the equations of motion. In the limit $v \to 0$, $G \to 0$, terms in $v^2$ may be dropped, so that $Q \approx \tilde{Q} \approx q \ll 1$. Then

$$\omega(q;v,G) \approx [v - G(1 + \eta k)]q - (1 + \eta k)q^3 . \tag{17}$$

When $\eta = 0$, i.e., when there is no diffusion in the low-temperature phase, one recovers the constitutional-supercooling result for the onset of instability, $v = G$. More generally, we can solve numerically for $G(v)$ and show that there is a maximum velocity $v_{max} = 1/k$ and a maximum temperature gradient $G_{max} \approx 1/16k$, above either of which the interface is always stable. In dimensional units, these limits are

$$v_{max} = \frac{D_I}{d_0} \frac{mc_0}{T_{N-I}} \frac{1-k}{k^2} \tag{18}$$

and

$$G_{max} \approx \frac{1}{16d_0} \frac{(mc_0)^2}{T_{N-I}} \frac{(1-k)^2}{k^3} f(k,\eta) , \tag{19}$$

The function $f(k,\eta)$ is of order unity over the range $0 < k < 1$ and $0 < \eta < 1$. One should note the strong variation of $v_{max}$ and $G_{max}$ with the partition coefficient. Typi-

cal solid-liquid transitions have $k < 0.1$, while typical nematic-isotropic transitions have $k \approx 0.9$. Changing the partition coefficient from 0.1 to 0.9 reduces $G_{max}$ by five orders of magnitude and $v_{max}$ by three orders.

We will make one final change of variables to rescale $v$ and $G$ to $v/v_{max}$ and $G/G_{max}$. This way, the experimental relevant values of $v$ and $G$ go from 0 to 1. Although one can derive an analytic expressions from $v_{max}$ [Eq. (18)], one can get only an approximate expression for $G_{max}$ [Eq. (19)]. Of course, numerically, there is no problem computing $G_{max}$ given parameter values. The bifurcation curve, calculated numerically, is plotted in Fig. 5.

One can interpret nicely the features of the bifurcation curve. The constitutional-supercooling limit corresponds to $l_D = l_T$, $l_C \rightarrow 0$. In this case, surface tension is irrelevant, and the diffusion of impurities takes place on a scale commensurate with that provided by the temperature gradient.

The maximum velocity occurs when $l_D = l_C$ and $l_T \rightarrow \infty$. Here, the thermal gradient is unimportant, and the interface is stabilized when the length scale associated with the destabilizing diffusion mechanism is comparable to the capillary length. Surface tension then kills the instability.

The maximum gradient occurs when $l_T \approx l_C$, where there is a crossover between the two stabilizing mechanisms, the temperature gradient and the surface tension. Since $l_D$ is also comparable to $l_T$ and $l_C$, it is hard to calculate $G_{max}$ analytically. Note that the expression for $G_{max}$ depends upon diffusion constants only through their ratio, $\eta$, and only weakly on this.

The enormous reduction of scale of the bifurcation curve is one of the most attractive features of working with liquid crystals. Whereas solid-liquid systems have $v_{max} \approx 1$ m/sec and $G_{max} \approx 10^7$ °C/cm, we can have nematic-isotropic systems with $v_{max} \approx 100$–$10\,000$ $\mu$m/sec and $G_{max} \approx 10$–$1000$ °C/cm. Quantitative exploration of the bifurcation curve on solid-liquid systems has been limited almost entirely to the $v \rightarrow 0$, $G \rightarrow 0$ limit, where

the Mullins-Sekerka theory is relatively well confirmed.[18] The only way so far to study the high-$v$, high-$G$ regime is through "flying-spot" experiments, whereby a laser or electron beam traverses the material at up to several meters per second.[19−21] Of course, under such circumstances, it is difficult to do any detailed modeling. Liquid crystals thus offer the intriguing possibility of exploring the entire $v$-$G$ parameter space in a single, well-controlled experiment. This was first pointed out by Caroli et al.[22]

Another result of linear stability analysis is a prediction of the critical wavelength at onset. Figure 6 plots the critical wave number $q_c$ as a function of the critical velocity $v_c$ along the bifurcation curve $G(v_c)$. Note that $q_c \rightarrow 0$ as $v_c \rightarrow v_{max} = 1/k$ within this model, and this limit can be inadequate. The maximum wave number $q_{max}$ is given by

$$q_{max} \approx l_C^{-1} \left| \frac{1-k}{2k^2} \right| g(\eta, k) \, , \qquad (20)$$

which confirms our earlier assertion that the smallest length scale over which pattern formation may occur is set by $l_C$. The function $g(\eta, k)$ is of order unity when $k \approx \eta \approx 1$. When $k \approx 0.9$, the factor $1 - k$ increases $\lambda_c$ by a factor of 10, or so. Further analytic details on the linear stability analysis may be found in the review by Coriell et al.[23]

## III. EXPERIMENTAL METHODS AND APPARATUS

This section is divided into three parts. The first discusses the materials studied. The second describes the construction of samples. The third describes the experimental apparatus itself, along with the techniques of data acquisition and analysis. For general references on the techniques followed, the works by Hunt et al., Esaki, Chopra, and Kaukler are useful.[24−29]
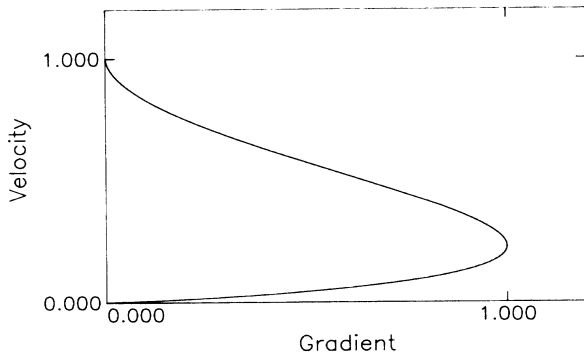
FIG. 5. Bifurcation curve $G(v)$. The axes of the plot are reversed because experimentally, the dependent variable is the temperature gradient. This curve is calculated for $k = 0.88$, $\eta = 0.53$. All other parameters are absorbed into $v_{max}$ and $G_{max}$, which are here scaled to 1.
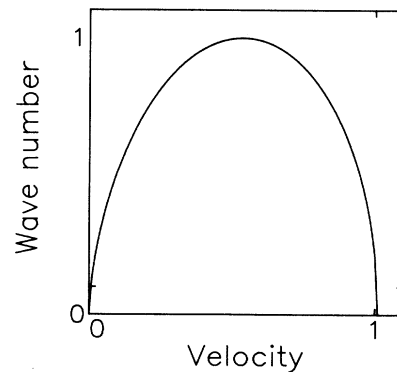
FIG. 6. Critical wave number vs critical velocity, as one moves along the marginal stability curve $G(v)$, as calculated from the Mullins-Sekerka theory. Same parameters as Fig. 5.

## A. Preparation of liquid crystals

One advantage of liquid crystals is that, at least for 8CB, they are "operationally pure" as recieved from the manufacturer, meaning that no experimentally achievable combination of velocity or temperature gradient led to a destabilization of the interface. It is necessary to add an impurity to see the Mullins-Sekerka instability.

To add impurities, about 500 mg of pure 8CB was transferred to a small bottle that had been carefully cleaned, dried, and weighed. The bottles were dried in an oven overnight at 120 °C. Chemical transfer occurred us-ing a clean magnet wire while the liquid crystal was in the nematic phase. An appropriate amount of impurity, on the order of a milligram, was then added while the bottle of liquid crystal was on a Mettler balance, sensitive to $10^{-5}$ g.[30] A clean Teflon stir bar ($2 \times 5$ mm$^2$) was add-ed permanently to the bottle for good mixing. After pre-paring each mixture of 8CB, the liquid crystal was pumped under vacuum in the isotropic phase for at least $\frac{1}{2}$ h to remove water and other volatile impurities. From the change in $G_{max}$, we estimated that the unpumped 8CB contained approximately 0.2 mol % volatile impuri-ties [the manufacturer notes that the saturation concen-tration of water in the $n$CB series is 0.15 mol % (Ref. 31)].

The choice of impurity was dictated by several criteria. The impurity should be an ideal one in the thermo-dynamic sense, both the melting and freezing points should be depressed linearly with the concentration of impurity. Any added material will satisfy these criteria for small-enough concentrations. The question is wheth-er the solution is ideal at concentrations large enough to be experimentally convenient ($c \approx 1$ mol %). Differential scanning calorimetry (DSC) measurements and visual ob-servation showed that our chosen impurity, hexa-chloroethane, only marginally meets those requirements. Finally, the physical parameters characterizing the im-purity should be known. In Sec. V A, below, we discuss the parameters for the 8CB-$C_2Cl_6$ system.

## B. Sample preparation

In general, the samples consisted of a thin "sandwich" of glass, the system or chemicals to be studied, and glass. The glass plates had to be treated to properly orient the nematic into a single domain. It was also important to keep the glass plates as parallel as possible.

For all samples, we began by cleaning the glass plates. The plates were first washed by rubbing them in an ap-proximately 2 vol % detergent-water solution (Micro Laboratory Cleaning Solution[32]), then rinsed for 15 sec under flowing distilled, deionized water, then placed in hot distilled, deionized water in an ultrasonic clean for 30 min, and placed in individual beakers (sized just larger than each plate so that the glass would stand nearly verti-cal, touching the beaker only along the bottom edge and the top two corners). Henceforth distilled, deionized wa-ter will be referred to as pure water. The beakers were filled with chromic-sulfuric acid (Fisher Glass Cleaning Solution[33]), which was heated to 100 °C for $4 \frac{1}{2}$ h on a hot

plate. The plates were rinsed by swishing them in pure water for 5 sec. They were then inserted into a new set of beakers filled with a 10 vol % HCl–water solution and were then soaked for 15 min. The purpose of the HCl solution was first to remove chromium ions from the glass surface, which are not well rinsed by water, and second to attach OH$^-$ groups to the glass surface to aid in the bonding of silane (see below). The glass plates were rinsed under flowing pure water for at least 10 min, then placed in an oven at 120 °C overnight to dry. Glass that was well cleaned showed no spots when dry.

The plates were then treated in order to align the liquid crystal perpendicular to the glass plates (homeotropic orientation). The techniques for achieving these orienta-tions have been much studied, for they are used to con-struct commercial liquid-crystal displays (LCD's).[34,35] The clean glass plates are dipped in a 1% silane solution dissolved in 1,1,1 trichloroethane (Merck ZLI 3124).[36] The silane solution as received contained many small par-ticles of undissolved silane in the trichloroethane. These are largely removed by filtering through a disposable, inorganic membrane, 0.2 $\mu$m syringe filter.[37] After dip-ping, the plates are exposed to air for 15 min and then baked at 120 °C for 10 min. The humidity in the room catalyzes the hydrolyzation of the silane onto the glass, forming a covalent bond between silicon groups on the surface of the glass and that in the silane molecule. Be-cause a very slight amount of water vapor is sufficient to hydrolyze the silane, the silane solution must only be opened to a N$_2$ atmosphere. We did all of our dipping in a nitrogen-filled glove box.[38]

The silane solution will deposit a monolayer on the glass surface, which will entangle the first layer of 8CB molecules, forcing them to stand perpendicular to the glass plate.[35] (See Fig. 7.)

The glass plates used in the experiment were of soda-lime float glass, cut by Glass-Tek Industries.[39] The bot-tom plate measured $24 \times 28 \times 1$ mm$^3$, the top plate $22 \times 22 \times 1$ mm$^3$. The overall lateral dimensions of the plates were chosen to given an aspect ratio of at least 100, where we define the aspect ratio to be the number of wavelengths of a typical pattern across the sample. The bottom plate needs to be somewhat larger than the top plate in order to assure good thermal contact with the copper ovens and an effective sample holder. The 1-mm thickness of the glass plates is a compromise between ri-gidity and time constant.

The plates were spaced by placing four small lengths of wire (either 12.5, 25, or 50 $\mu$m) between them and putting
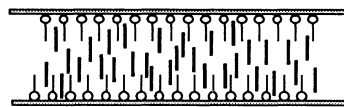


FIG. 7. Homeotropic anchoring. Silane molecules are bond-ed to the surfaces of the glass plates (shown shaded). The hy-drocarbon tails of the silane molecules entrain the 8CB, orient-ing the liquid crystal perpendicular to the glass plates.

two drops of epoxy (Devcon[40]) on each wire. By counting interference fringes from a fluorescent light, the angle between the two plates was typically measured to be $(1-2) \times 10^{-4}$ rad. In order to make the plates as parallel as possible, we constructed a brass jig that allowed us to adjust the pressure on the top plate by tightening and loosening screws. The epoxy should dry at room temperature. If it cures at high temperatures, it changes dimension, warping the glass plates. The limiting factor in making the plates parallel seems to be the rigidity of the plates and glue rather than the flatness of the plates themselves.

The assembled cell was then placed on a hot plate at about 60 °C, and the sample was then filled by placing drops of liquid crystal at one corner and relying on capillary action to draw the chemical between the plates. To avoid dust, we assembled the samples in a laminar-flow hood.[41]

### C. Apparatus

The completed cells were mounted in a temperature-gradient stage, adapted from the original design of Jackson and Hunt.[24] (See again Fig. 1.) Two temperature-controlled ovens are separated by a small 4-mm gap. The sample straddles the gap, imposing a linear temperature gradient across the material to be studied. The large thermal conductance of the 1-mm-thick glass plates of the sample ensures that the temperature gradient is imposed on the cell. The temperatures are chosen so that an interface between two phases appears in the gap, where it is observed via a microscope. The sample is then pushed slowly by a motor at constant speed across the gap. To a first approximation, the temperatures in the glass plates will readjust adiabatically so that the temperature gradient is fixed in the laboratory frame of reference. The interface will thus remain in its original location in the gap. In the reference frame of the sample, it is moving at a velocity equal and opposite to the velocity of the sample. Thus, we can observe an interface propagating at a controllable velocity while moving along with that interface.

Next, we review some of the points considered in the design of the stage. The ovens should be as large as possible to provide the largest possible thermal mass. We used copper plates anchored to larger copper blocks. The use of thin copper plates was dictated by the need to permit microscope observations by objectives with working distances as short as 5 mm. The larger blocks compensated for the small mass of the plates. One oven was heated by an electrical heater, connected to a proportional, integrating, and differentiating (PID) feedback loop, controlled by an Omega CN-9000 temperature regulator hooked up to a platinum resistance temperature device (RTD) (Omega F3105).[42] Its useful range was 30–150 °C, with stability of 0.1 °C over the long term and 0.03 °C over the short term (10 min). The other oven was regulated by circulating temperature-controlled water through the large copper block. Its useful temperature range was −30 °C to 90 °C. (Temperatures lower than 5 °C could be achieved by adding ethylene glycol to the water bath.) The water bath was a Neslab RTE-8DD cir-

culator, with short-term stability of 0.01 °C and long-term stability of 0.1 °C (determined by changes in the room temperature).[43] In order to avoid a vertical temperature gradient, we suspended thermally linked top plates 0.2 mm above the sample.

The ovens were separated by 4.00 mm and the sample placed between them in a fiberglass holder that featured a rotatable cutout for the sample in the center. The holder was spring-loaded at the sides and front. The side spring loading compensated for the thermal expansion of the fiberglass over the temperature gradient. Small Teflon pads gave stick-free motion against the copper side walls. The front spring allowed the sample to be pushed in both directions. (See Fig. 8.)

The stage was pushed by a fine screw (Newport AJS-1).[44] The screw was driven by a Berger Lahr stepping motor (RDM 566/550, with Divistep controller), with a resolution of 500–10 000 steps/revolution.[45] The motor-screw combination gave velocities ranging from 0.1 to 300 $\mu$m/sec. The absolute accuracy of the velocity was far from being the limiting factor of experimental precision.

The temperature gradient was calibrated by constructing a dummy cell with a thermocouple inside (3 mil Teflon-coated, Chromel-Alumel wires, Type E, spot welded together) and running it across the gap at various velocities. The cold junction was referenced to the cold oven block, and the temperature difference was recorded directly by a Keithley 195 voltmeter interfaced to a Hewlett-Packard 9816 computer.[46] A typical run is shown in Fig. 9. The run started 4 mm before the gap and finished 4 mm after the gap. The gap runs from 4 to 8 mm on the scale of Fig. 9. The major conclusions were that at even the highest velocities, the temperature gradient was a constant over the central 80% of the gap; however, because of thermal short-circuiting of the ovens by the glass plates, the actual temperature gradient was calibrated to be only about three-fifths the naive value, $G_0$, defined to be the difference between the oven temperatures divided by the oven separation.

The temperature-gradient stage was mounted on an inverted microscope (Olympus IMT-2).[47] An inverted microscope was chosen because it provides a large, stable workspace to mount the heavy stage (5 kg). Much of the
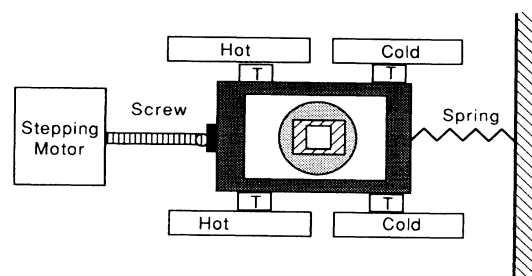


FIG. 8. Diagram of experimental apparatus. A top view is shown, with the top and bottom plates not depicted. The four rectangles marked "T" are blocks of Teflon. The sample is shown in the middle of the figure. Note the rotatable sample holder.
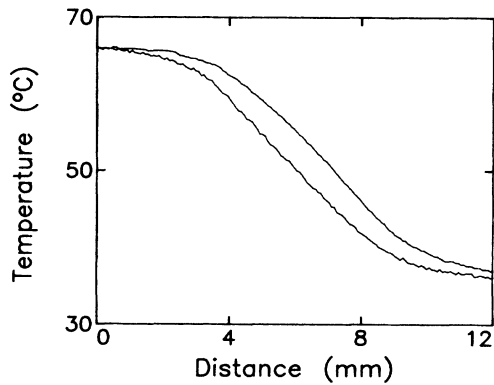
FIG. 9. Horizontal temperature profile in sample. The profile was generated by running a dummy cell with a thermocouple through the apparatus. The profile varied with velocity, as shown by scans at $v=1$ and 80 $\mu$m/sec, lower and upper curves, respectively. The gap between the two plates started at $x=4$ mm and ran to $x=8$ mm.



FIG. 10. Experimental bifurcation curve. The concentration $c_0=0.46$ mol %, $d=55$ $\mu$m.

For a typical nematic-isotropic sample, $D \approx 10^{-7}$ cm$^2$/sec, $v \approx 10$ $\mu$m/sec, and $k=0.9$. This gives $N \approx 10^4$.

stability comes because the objectives move when focusing, while the stage is bolted to the microscope frame. The temperature-gradient stage was connected to an $XY$ table (Ealing 22-8171),[48] which was also bolted to the microscope frame. Micrometer screws permitted horizontal movements with better than 10-$\mu$m precision. The $XY$ table was used both for positioning and for measurement.

At various times, we used bright-field, dark-field, phase contrast, polarization, and Nomarski differential interference contrast. We measured the shape of the interface under bright-field illumination because it shows only the interface, which appears as a sharp line. Phase contrast increases the contrast of the interface against the background, at the cost of some resolution. Crossed linear polarizers allowed us to probe details of the alignment of molecules in the optically anisotropic nematic. Nomarksi illumination was useful for its shallow depth of field ($\approx 2$ $\mu$m), which allowed us to scan even thin cells vertically and measure sample-thickness profiles.

Our run procedure was as follows: new cells were run their entire length at 5 $\mu$m/sec (or some speed slow enough to keep a stable interface) in order to push loose dust to one side of the cell. We often had to repeat the procedure 4 or 5 times until the sample had "cleaned itself." This procedure was fairly effective.

Once the cell has been "cleaned," we begin to use it immediately. One important advantage of liquid crystals is that their high critical velocities (1–100 $\mu$m/sec), combined with a partition coefficient close to 1 means that only small amounts of impurities are displaced during the experiment. Thus one does not need to let the system diffuse back to equilibrium. More precisely, the number of passes to produce a 2:1 difference in impurity levels at one end of the cell compared to the other is approximately

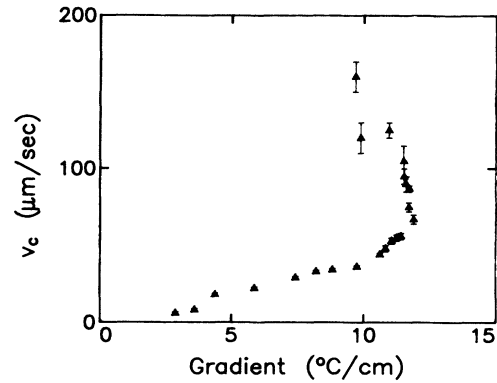$$N \approx \tfrac{1}{3} L_{\text{sample}} \frac{v}{D} \frac{k}{1-k} . \qquad (21)$$

## IV. EXPERIMENTAL RESULTS

The most basic test of the Mullins-Sekerka instability is to determine under what conditions a flat interface loses its stability and what is the most unstable wave number ($q_c=2\pi/\lambda_c$) at the onset of instability. The predictions of the Mullins-Sekerka theory for these questions were discussed in Sec. II B and the results are summarized in Figs. 5 and 6.

Our measurements of those curves are shown in Figs. 10 and 11. Qualitatively, they agree with the theoretical prediction. In particular, we observe a maximum temperature gradient $G_{\max}=11.9$ °C/cm, beyond which the interface is stable for all accessible velocities. Despite qualitative agreement between Figs. 5 and 10 and between Figs. 6 and 11, attempts to fit the data lead to unacceptable values of the physical parameters characterizing the sample. Taking results from Sec. V A, we estimate the parameter values, along with their uncertainties
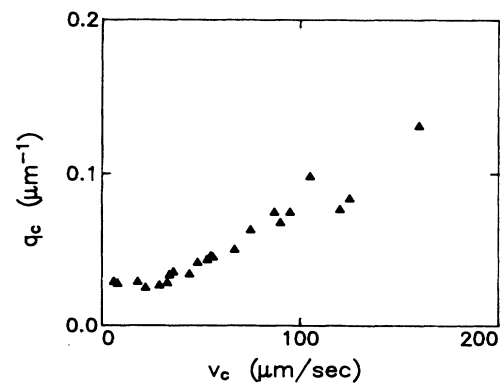


FIG. 11. Wave number at onset vs velocity. $c_0=0.46$ mol %, $d=55$ $\mu$m.

and conclude from independent experiments that the partition coefficient $k$ ranges between $0.86 < k < 0.93$, the absolute value of the liquidus slope $m$ falls in the range $0.9 < m < 1.3 \,°C/mol \%$, the diffusion constant of $C_2Cl_6$ in the nematic phase in homeotropic alignment is $D_{N,perp} = 2 \times 10^{-7}$ cm$^2$/sec, the diffusion constant of $C_2Cl_6$ in the isotropic phase is $D_I = 4 \times 10^{-7}$ cm$^2$/sec, and the thermal capillary length $d_0 = 4.7 \pm 2.2 \times 10^{-10}$ cm.

These values predict at $G_{max}$ the following values: $G = 230$–$2600 \,°C/cm$, $v = 230$–$760$ $\mu$m/sec, and $\lambda = 0.4$ –$1.2$ $\mu$m. In contrast, we measure $G = 11.9 \,°C/cm$, $v = 67$ $\mu$m/sec, $\lambda = 125$ $\mu$m. The wide range of predicted values follows from an extreme sensitivity to the value of $k$. (See Sec. II B, above.)

It has been pointed out that elastic deformations of the nematic director field may play a role in our experiments.[49] A length scale $d_1 = (K/L)^{1/2}$, where $K$ is an elastic constant and $L$ is latent heat, is on the order of 10 Å for our system, however, substituting this for $d_0$ does not resolve the theory with the experiments, so it is yet unclear how relevant this length scale may be.

We can take a slightly different approach and ask what parameter values give a good fit to the experimental data. Letting $k$, $D_I$, and $d_0$ be free parameters, we get an approximate fit with $k = 0.851$, $D_I = 1 \times 10^{-5}$ cm$^2$/sec, and $d_0 = 1.4 \times 10^{-8}$ cm. The value of $k$ is acceptable, that of $D_I$ is 25 times too high, and that of $d_0$ is 500 times too high, so clearly we have been neglecting some relevant physics.

Until this point, we have discussed the equations as if the samples were only two dimensional. Our evidence for an inverted meniscus[1] and a solute-driven convective roll suggest that the third dimension plays an important roll. The solute-driven convective roll we observe on the isotropic side of the interface will certainly enhance impurity transport away from the interface, thus increasing the apparent or operational diffusion constant $D_I$ by a factor of 10 (see Sec. V B for details). Furthermore, the existence of a convective roll possibly brings a new and fourth length scale to the problem. If we define $l$ to be the length scale associated with the roll, then possibly the capillary length could be rescaled to $d_0' \approx (d_0 l)^{1/2}$. Thus if $l$ is of the order of 20 $\mu$m, this implies a $d_0' \approx 100$ Å. This is a plausible explanation, but is not theoretically tested. To test the importance of the third dimension, we looked at a sample with varying thickness and for thickness below 5 $\mu$m; a reasonable agreement with theory is observed.

## V. TECHNICAL ANALYSIS

Here we take a closer look at the detailed technical analysis of the physical constants associated with the system. First we review previous experiments bearing on these quantities for our system. Then we discuss in Sec. V B the solute-driven convection in detail. Since the third dimension is clearly important in our system, we end the analysis with a look at the thickness dependence of the experiment.

## A. Estimates of parameter values

The average concentration of impurities $c_0$ is for our experiments nominally 0.46 mol % hexachloroethane ($C_2Cl_6$) in 8CB. The figure is determined by direct weighing of impurity and host during the preparation of the mixtures. We believe that these values should be accurate to about 10%, the accuracy of the scales used to weigh the chemicals. (Typical mixtures used about 500 mg 8CB and a few mg $C_2Cl_6$.) As for other impurities, we note that the primary contaminant in the 8CB as received from the manufacturer is water,[31] which has a saturation concentration of $c_{water} \approx 0.15$ mol %. This water is removed by pumping under vacuum in the isotropic phase.

The temperature-concentration phase diagram is characterized by the slopes of the liquidus and solidus lines [see Fig. 4(b)]. In place of the latter, we can use the partition coefficient $k$ (the ratio of liquidus to solidus slopes). Although the value of the partition coefficient for $C_2Cl_6$ in 8CB is yet to be measured, the phase diagram of 8CB with a large number of nonmesomorphic solvents has been studied.[50] For 13 cases, the partition coefficient ranged between 0.73 and 0.93. If one restricts oneself to short rodlike impurities (like $C_2Cl_6$), then the range was 0.86 to 0.93.

Knowing $k$, one can calculate the slope $m$ of the liquidus line. From Sec. II, we have the relation

$$m = \frac{RT_{N\text{-}I}^2}{L}(1-k) \; . \tag{22}$$

If one plots $m$ versus $k$ for the impurities measured by Ghodbane and Martire,[50] the points are well fit by a straight line, although the $x$-intercept differs from 1 slightly ($1.08 \pm 0.03$). The magnitude of the slope is $m_0 = 5.7 \pm 0.7 \,°C/mol \%$. Equation (22) predicts that $m_0 = 13.4 \pm 0.5 \,°C/mol \%$. (In computing $m_0$, we have used the value of the latent heat measured by Marynissen et al.,[51] as described below.) In computing $m$, however, we shall use the least-squares fit $m = 6.2 - 5.7k$ to get the liquidus slope. For $0.86 < k < 0.93$, this gives $1.3 > m > 0.9 \,°C/mol \%$ as estimates for the liquidus slope.

We also need the values of the diffusion constants of $C_2Cl_6$ in the nematic and isotropic phases of 8CB, near $T_{N\text{-}I}$. Although these have not been measured for $C_2Cl_6$, there is data on the self-diffusion of 8CB and on the diffusion of methyl red in 8CB. Experimentally, the diffusion constants that have been measured obey Arrhenius laws, of the form $D = D_0 e^{-E_a/RT}$, where $E_a$ is an activation energy which can loosely be thought of as the probability for an impurity molecule to hop into an adjacent "hole" in the liquid.[52] A conclusion one can draw from this is that for dilute solutions, at a given temperature, the diffusion constants will depend primarily on the molecular weight of the impurity. For 8CB, this is 291.2, for methyl red,[53] it is 269.31, while for $C_2Cl_6$, it is 236.74. We thus assume that the diffusion constants are (at least roughly) the same. For methyl red, Takezoe et al.[54] measure via forced Rayleigh scattering that

$D_{N,\text{parallel}} = 2.6 \times 10^{-7}$ cm$^2$/cec, $D_{N,\text{perp}} = 2.0 \times 10^{-7}$ cm$^2$/sec, and $D_I = 3.8 \times 10^{-7}$ cm$^2$/sec (at $T_{N-I}$). Here again, the subscript $N$ denotes the nematic phase, while $I$ denotes the isotropic phase. The rodlike structure of 8CB leads to two different diffusion constants, one parallel to the long axis, the other perpendicular. For 8CB, Moseley et al.[55] measured via NMR pulsed-gradient spin-echo techniques, $D_I = 5.2 \times 10^{-7}$ cm$^2$sec. Ghosh and Tettamanti[56] obtain $D_I = 4.6 \times 10^{-7}$ cm$^2$sec by the same method. Since the sample is homeotropic, we take $D_{N,\text{perp}} = 2 \times 10^{-7}$ cm$^2$/sec and $D_I = 4 \times 10^{-7}$ cm$^2$/sec. Although the precise values may differ somewhat, we expect the order of magnitude and the ratio $\eta = D_N / D_I \approx 0.5$ should hold.

The final parameter is the thermal capillary length $d_0$ defined in Sec. II. The surface tension has been measured[57] by the sessile-drop method to be $0.95 \pm 0.4 \times 10^{-2}$ erg/cm$^2$. Although the value of the surface tension is small and the error large, the result is well corroborated by independent measurements on different materials.[57-60] All of these measurements give $\gamma_{N-I} = O(10^{-2})$ erg/cm$^2$.

Values of the latent heat of the nematic-isotropic transition have been measured often, usually by differential scanning calorimetry. The published results range from 6

to $12 \times 10^9$ erg/mol.[61] Ratna and Chandrasekhar[62] have recently traced the source of the discrepancy and confirm the value Marynissen et al.[51] obtained: $L_{N-I} = 6.12 \pm 0.05 \times 10^9$ erg/mol.
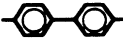
Using the above values of $\gamma$ and $L$ and the tabulated values of $M_w$ and $\rho_N$ (see Table I, below), we obtain a thermal capillary length of $d_0 = 4.7 \pm 2.2 \times 10^{-10}$ cm. Although a value of $d_0 = O(10^{-2})$ Å may seem surprising, one can show (see Appendix) that $d_0$ becomes very small for weakly first-order phase transitions.

A final confirmation of these ideas comes from a direct measurement of $d_0$ in the liquid crystal PAA. Armitage and Price[63] showed via differential scanning calorimetry that the nematic-isotropic transition of PAA is depressed by about $0.1\,°C$ when the liquid crystal is absorbed in porous silica of pore size $R \approx 100$ Å. This may be due to curvature of the $N$-$I$ interface, however, it gives

$$d_0 \approx \left| \frac{\Delta T}{T_{N-I}} \right| \frac{R}{2} \approx \frac{0.1}{400} \frac{10^{-6}}{2} \approx 10^{-10} \text{ cm} , \qquad (23)$$

supporting the unusually small values of $d_0$ inferred above.

TABLE I. Properties of 8CB, both general and those specific to the nematic-isotropic transition.

| | Quantity | Symbol | Value | Units | Ref. |
|---|---|---|---|---|---|
| General | Chemical name | | 4,4'-$n$-octylcyanobiphenyl | | |
| | Structure | | $C_8H_{17}$ —◯—◯— CN | | 61 |
| | Molecular weight | $M_{8CB}$ | 291.2 | g/mol | 31 |
| | Chemical abstracts No. | $RN$ | 52709-34-9 | | |
| $N$-$I$ transition | Transition temperature | $T_{N-I}$ | 40.5 | °C | 61 |
| | Pseudo-second order point | $T_{N-I} - T^*$ | $2.0 \pm 0.3$ | °C | 72 |
| | Latent heat | $L$ | $(6.12 \pm 0.05) \times 10^9$ | erg/mol | 51 |
| | First Landau coeff. | $a$ | $(1.9 \pm 0.1) \times 10^6$ | erg/cm$^3$°C | 72 |
| | Correlation length | $\xi$ | $(70^{+70}_{-40}) \times 10^{-8}$ | cm | 57 |
| Bulk prop. at $T_{N-I}$ | Density | $\rho_N$ | $0.979\,96 \pm 0.0002$ | g/cm$^3$ | 73 |
| | | $\rho_I$ | $0.978\,31 \pm 0.0002$ | | |
| | Elastic constants | $K_{11}$ | $(1.2 \pm 0.1) \times 10^{-7}$ | dyne | 74 |
| | | $K_{22}$ | $(1.9 \pm 0.1) \times 10^{-7}$ | | |
| | | $K_{33}$ | $(2.4 \pm 0.1) \times 10^{-7}$ | | |
| | Viscosity | $\eta$ | $(3.0 \pm 0.3) \times 10^{-2}$ | Poise | 75 |
| $N$-$I$ interface | Surface tension | $\gamma$ | $0.0094 \pm 0.004$ | erg/cm$^3$ | 57 |
| | Thermal capillary length | $d_0$ | $(4.7 \pm 2.2) \times 10^{-10}$ | cm | this work |
| | Surface anchoring coeff. | $W$ | $(8.5 \pm 2.1) \times 10^{-4}$ | erg/cm$^2$ rad$^2$ | 76 |
| | Tilt angle | $\theta_t$ | $48.5 \pm 6$ | deg | 76 |
| Binary phase | Mol. wt. $C_2Cl_6$ | $M_{C_2Cl_6}$ | 236.74 | g/mol | 77 |
| | Liquidus slope | $m$ | 1.35 | °C/mol % | this work |
| | Partition coefficient | $k$ | 0.85 | | this work |
| | Chemical diffusivity | $D_{N_\parallel}$ | $2.6 \times 10^{-7}$ | cm$^2$/sec | 54 |
| | | $D_{N_\perp}$ | $2.0 \times 10^{-7}$ | | |
| | | $D_I$ | $3.8 \times 10^{-7}$ | | |

## B. Convection in detail

Although we have considered the physical parameters of the system, we must now look closely at the missing physical process we have identified as solute-driven convection. Roughly, the buildup of impurities on the liquid side of the interface leads to a heavy layer of fluid. Because the density gradient is horizontal (i.e., perpendicular to gravity), convection starts with a zero onset Rayleigh number. An obvious effect of such convection will be a larger $D_I$ because of the enhanced transport of impurities away from the interface. Less obvious effects will be described, below.

The presence of convection may be established directly by looking for dust particles in front of the interface. Most dust particles are either too heavy to be moved by the isotropic fluid or are pinned to the glass plates. Occasionally, however, we are able to see dust particles moving along with the fluid flow. Observing such particles, we conclude that there is a single convective role parallel to and immediately in front of the interface.

The first step is to justify our claim that the convection is driven by the buildup of impurities in front of the interface. Other possibilities include thermally driven convection and impurity-driven convection caused by the Soret effect.

In all cases, convection is a competition between buoyancy (the driving force) and diffusion (the dissipative force). In thermal convection, the buoyancy is supplied by the expansion of the fluid in response to temperature changes. Typically, hot fluid is lighter and rises. The amount of convection is quantified by the Rayleigh number

$$\mathcal{N}_{Ra} = \frac{Gd^4\alpha g}{\nu\kappa} \ . \tag{24}$$

Here, $G$ is the temperature gradient, $d$ the plate spacing, $\alpha = -(1/\rho)(\partial\rho/\partial T)$ the thermal expansion coefficient, $g$ the acceleration due to gravity, $\nu = \mu/\rho$ the kinematic viscosity, and $\kappa$ the thermal diffusivity. Typical values for 8CB in our experiment are (in cgs units) $G \approx 10$, $d \approx 3 \times 10^{-3}$, $\alpha \approx 10^{-3}$, $g \approx 10^3$, $\nu \approx 10^{-2}$, and $\kappa \approx 10^{-3}$. This leads to $\mathcal{N}_{Ra} \approx 10^{-4}$. This is seven orders of magnitude smaller than the Rayleigh number needed to initiate convection with a vertical gradient. However, in a horizontal gradient, the critical $\mathcal{N}_{Ra} = 0$.

Next, we consider solute-driven convection. The control parameter is again the Rayleigh number, except that now the buoyancy terms are due to the concentration dependence of the fluid density. Thus we have

$$\mathcal{N}_{Ra}^S = \frac{\nabla c d^4 \beta g}{\nu D_I} \ . \tag{25}$$

Here, the concentration gradient $\nabla c$ replaces $G$, $\beta = (1/\rho)(\partial\rho/\partial c)$ replaces $\alpha$, and $D_I$ replaces $\kappa$. Evaluating $\nabla c$ at the interface [see Eq. (13)] we have

$$\mathcal{N}_{Ra}^S = \frac{vc_0\left[\dfrac{1-k}{k}\right]d^4\beta g}{\nu D_I^2} \ , \tag{26}$$

where $v$ is the interface velocity. In cgs units, $v \approx 10^{-3}$ to $10^{-2}$, $c_0 \approx 10^{-2}$, $(1-k)/k \approx 10^{-1}$, $d \approx 3 \times 10^{-3}$, $\beta \approx 1$, $g \approx 10^3$, $\nu \approx 10^{-2}$, $D_I \approx 4 \times 10^{-7}$. We arrive at

$$\mathcal{N}_{Ra}^S \approx 10\text{--}10^2 \ . \tag{27}$$

Thus solute-driven convection is more important than thermal-driven convection: $\mathcal{N}_{Ra}^S/\mathcal{N}_{Ra} \approx 10^5$.

A final possibility is that the temperature gradient will induce a concentration gradient via the Soret effect. The magnitude of the induced concentration gradient is given by

$$\nabla c_{Soret} \approx \frac{k_{Soret}}{T}G \approx \frac{3}{300}(10) \approx 0.1 \ \text{cm}^{-1} \ , \tag{28}$$

where we have chosen $k_{Soret} = 3$ as representative of the largest observed values of the Soret coefficient for organic molecules.[64] By contrast,

$$\nabla c_{MS} \approx c_0\left[\frac{1-k}{k}\right]\frac{v}{D_I} \approx 10 \ \text{cm}^{-1} \ , \tag{29}$$

so that the Soret effect is negligible.

The above discussion leads us to expect that the Rayleigh number quantifying solute-driven convection depends linearly on velocity. Studying the motion of a dust particle in a convective roll, one indeed sees that the roll velocity depends on the front velocity (see Fig. 12). The $y$ axis is the inverse of the time for the particle to complete one cycle. The interpretation is complicated because sometimes the dust particle follows the roll's motions and traces out a circle in the vertical plane. At other times, the particle seems to be caught at the center of the roll and tumbles in place. The latter motion is more rapid than the former. This is not surprising, as we expect the convection roll to spin fastest at its center and then to slow down as we approach the interface or the glass plates, where the flow velocity must vanish. Once we separate the two motions, roll and spin, we see indica-
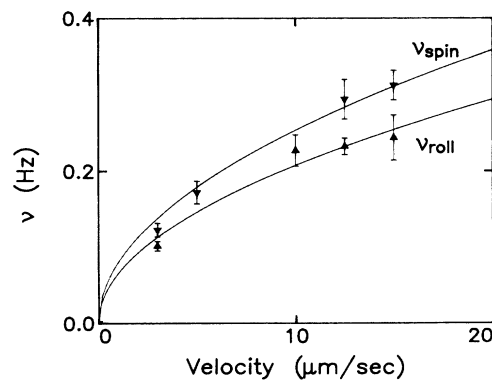


FIG. 12. Convective motion of a particle in front of the interface. The frequency plotted on the $y$ axis is the inverse of the time for the particle to make one revolution. The velocity $v$ is that of the interface. $G = 36\,°\text{C/cm}$, $c_0 = 1.56$ mol % D37 dye in 8CB, $d = 28 \ \mu\text{m}$.

tions that the flow velocities versus front velocity fall on curves that may represented by a power law, with $\alpha = 0.53 \pm 0.03$, different from a recent model.[65]

Concentration gradients building up at the interface also account for the observation of only one convective roll, on the isotropic side of the interface. Further away from the interface, the concentration gradient drops to zero. On the nematic side, we do not see any convection, the impurity gradients being much smaller.

An obvious effect of convection is to enhance impurity transport away from the interface. The roll will homogenize impurities over the length scale $d$, leading to a much larger effective diffusion constant for the isotropic phase:

$$D_{\text{eff}} \approx dv_{\text{fluid}} \approx d\frac{D_I}{d}(\mathcal{N}_{\text{Ra}}^S)^\alpha = D_I(\mathcal{N}_{\text{Ra}}^S)^\alpha , \qquad (30)$$

where the experimental value of $\alpha$ is close to 0.5. Since $\mathcal{N}_{\text{Ra}}^S = O(100)$, we expect diffusion to be enhanced by a velocity-dependent factor, of order 10. Theoretically the value for $\alpha$ is unclear.[66,67]

An enhanced value of the diffusion coefficient on the isotropic side cannot account for the observed values of $G_{\text{max}}$ and $q_c$. For example, $G_{\text{max}}$ depends on $D_I$ only through the quantity $1 + k\eta$, whose value changes only from 1.4 to 1.0 as $\eta = D_N/D_I$ is decreased from 0.5 to 0.0.

The most likely possibility is that convection alters the form of the dispersion relation and introduces the plate separation as a fourth relevant length scale in the problem. When two instabilities interact, as they do here (recall that the convection is driven by the impurity gradients generated by the interfact motion), one may be strictly forced to follow the other. For example, Caroli et al.[68] have studied the coupling of solute-driven convection in the case of a vertical solute gradient, where convection begins at finite $\mathcal{N}_{\text{Ra}}^S$. They find that the values of the Mullins-Serkerka instability are barely changed, while the values of the onset of the convective instability are radically altered. In our case, the reverse seems to occur. Convection starts at zero velocity and therefore may affect the finite values of velocity needed to initiate the Mullins-Sekerka instability.

### C. Dependence upon thickness

To test some of the above ideas, we looked at the effects of thickness on the interface. The experiments were performed in a variable thickness cell made by placing a 25-$\mu$m spacer along a single edge. The inset to Fig. 13 shows the thickness profile. As shown, the profile is well fit by a parabola, which was used in calculating the thickness of the cell at a given position.

We placed the cell in the directional solidification apparatus so that the thickness gradient was parallel to the interface. This allowed us to scan a continuous range of thickness during each run. Since the angle between the glass plates is small (about $2 \times 10^{-3}$ rad, maximum), we may safely take each region as having locally parallel plates of variable $d$.

Figure 13 shows the critical onset velocity versus thickness. Here we see for a small value of $G$
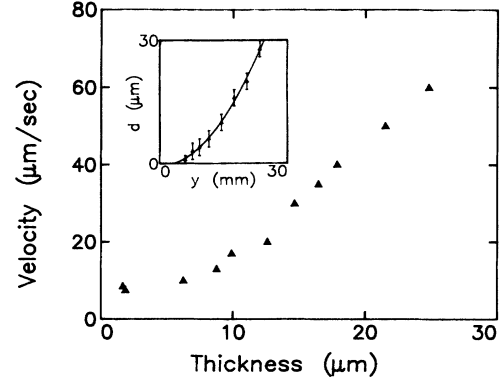


FIG. 13. Critical velocity vs thickness. Inset shows the sample thickness profile, as measured by Nomarski optics. $G = 22\,°C/cm$, $c_0 = 0.61$ mol %.

($G \ll G_{\text{max}}$) that $v_c$ is independent of thickness for $d \leq 5$ $\mu$m and that it rises approximately linearly with thickness thereafter. Figure 14 measures the onset wavelength for varying thicknesses. In practice, the curve is generated by fixing the gradient and varying the velocity.

At the thinnest plate spacings (2–3 $\mu$m), the values of $v_c$ and $\lambda_c$ approach those expected from the simple Mullins-Sekerka theory. Specifically, from the bare parameters, we predict (for $G = 17\,°C/cm$) $v_c = 1.2$ $\mu$m/sec, $\lambda_c = 28 \pm 12$ $\mu$m, and we measure $v_c = 5 \pm 1$ $\mu$m/sec, and $\lambda_c = 15 \pm 4$ $\mu$m. The uncertainty in the predicted values comes from the uncertainty in the surface tension alone. Some of the disagreement may come from errors in $m$, $D_N$, and $D_I$. In addition, convection, while greatly reduced in importance, may not be entirely negligible at these thicknesses, where $\mathcal{N}_{\text{Ra}}^S \approx 1$. When $\mathcal{N}_{\text{Ra}}^S \approx 1$, the diffusion time $d^{2/D}$ will be comparable to the roll turnover time $(d^{2/D})(\mathcal{N}_{\text{Ra}}^S)^\alpha$ so that we may regard the mass transport due to convection as comparable to that transported via diffusion. In order that convection be truly negligible, we would need $\mathcal{N}_{\text{Ra}}^S \ll 1$.
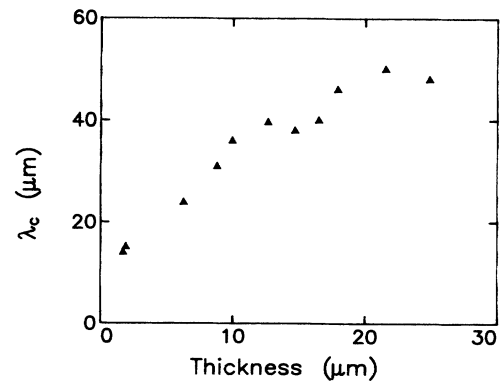


FIG. 14. Onset wavelength vs thickness. $G = 17\,°C/cm$, $c_0 = 0.61$ mol %.

## VI. CONCLUSION

In the preceding section, we have seen that the presence of solute-driven convection in the fluid complicates theoretical interpretation of results. On the other hand, convection eases the experimental burden. If there really were no convection, we believe that wavelengths would be very small.

These experiments raise a number of questions. For the theorist, the challenge is whether one can build a comprehensive model to account, at least in a general way, for the observations described here. Such a model would supplement the usual Mullins-Sekerka formulation with flow equations in the isotropic phase. Another complication that we have not discussed in this paper but that must also be considered is the effect of elastic forces in the nematic phase. As mentioned in our previous work,[1] there is a singularity in the director field in the nematic phase. At present, elastic effects have not been considered much.[49]

On the experimental side, we can try to find a system where convection is reduced but where the Mullins-Sekerka instability is observable over the entire parameter range, i.e., where we can reach $v_{max}$ and $G_{max}$. One can reduce convection by density-matching the impurity with the host molecule. The density difference between 8CB and $C_2Cl_6$ is close to 100%. Since $\rho_{8CB} \approx 1$, it should be possible to find an impurity that matches the one of 8CB to 1% or so. We can also reduce the sample thickness. Using evaporated metal as spacers, samples of 1–2 $\mu$m thickness become possible.

A remaining problem is that the generic impurity, density matched or not, will have a partition coefficient $k$ of $0.8 \pm 0.1$, which implies a large $v_{max}$ and $G_{max}$ and small $\lambda$. To bring these values down to something reasonable, we should have $k$ closer to 1. A way to do this is to pick an impurity that is chemically very close to 8CB, for example another member of the $n$CB series. The densities of molecules in this family are matched to within 5%, for $n = 5$–9. Neighboring series members are matched as close as 0.5%. Presumably, by varying the hydrocarbon chain length, we can vary $k$ as well.

### ACKNOWLEDGMENTS

### APPENDIX: THE CAPILLARY LENGTH IN THE LANDAU–de GENNES THEORY, OR WHY $d_0$ IS SO SMALL

In this appendix, we show how the small values of the thermal capillary length $d_0$, of order $10^{-2}$ to $10^{-1}$ Å, may be understood in terms of the Landau–de Gennes theory of the nematic-isotropic transition.[69–71] If we consider a flat interface, the order parameter $Q_{ij}$ will vary only along the direction normal to the interface, which is defined to be the $y$ axis. The nematic ordering will further be assumed to be along the $z$ axis, as it is in the case of homeotropic samples. We will neglect the distortions in the director field of the nematic that arise because of the finite tilt angle $\theta_t$ at the interface. In this simplified geometry, where $Q_{zz} = Q$, $Q_{xx} = Q_{yy} = -Q/2$, $Q_{xy} = Q_{yz} = Q_{xz} = 0$, the order parameter $Q$ is a scalar and hence, the van der Waals approximation is identical to that of a liquid-vapor transition.

Within such a square-gradient approximation, the surface tension is given by the excess free-energy density $F$,

$$\gamma = \int_{-\infty}^{+\infty} F\left[ Q(y), \frac{\partial Q(y)}{\partial y} \right] dy , \tag{A1}$$

where the integral is to be evaluated over the $Q(y)$ which minimizes $F$ and we write the free-energy functional in the form

$$F = \tfrac{1}{2}AQ^2 - \tfrac{1}{3}BQ^3 + \tfrac{1}{4}CQ^4 + \tfrac{1}{2}a\xi_0^2 T^* \left[ \frac{\partial Q}{\partial y} \right]^2 , \tag{A2}$$

where $A$, $B$, $C$, and $\xi_0$ are phenomenological coefficients whose values must be determined empirically. Also, we assume as usual that the only temperature dependence of the coefficients is that of $A$, which is of the form $A = a(T - T^*)$, where $T^*$ is the temperature at which a second-order phase transition would occur if $B = 0$ exactly. The quantity $\xi_0$, the bare correlation length, is introduced in Eq. (A2) in anticipation of future results. It is typically a molecular dimension, roughly several angstroms.

To find the conditions describing a first-order transition, we recall that the free energy must be minimized, so that $\partial F/\partial Q = 0$. To have coexistence between the nematic and isotropic phases, we need $F(Q_{N-I}) = F(0) = 0$, where $Q_{N-I}$ is the value of the order parameter in the nematic phase at the transition temperature $T_{N-I}$ and $Q = 0$ in the isotropic phase. Note that the temperature $T_{N-I}$ is different from the phantom second-order transition temperature $T^*$. Indeed, imposing $\partial F/\partial Q = F = 0$, we obtain

$$T_{N-I} - T^* = \frac{2}{9} \frac{B^2}{aC} , \tag{A3}$$

$$Q_{N-I} = \frac{2}{3} \frac{B}{C} . \tag{A4}$$

The nematic-isotropic transition can thus be seen as an interrupted second-order phase transition. If $B$ were zero, we would have $T_{N-I} = T^*$ and the transition would be second order. Instead, the divergence of thermodynamic quantities halts at $T = T_{N-I}$, where the order parameter jumps discontinuously from $Q = 0$ (the isotropic phase) to $Q = Q_{N-I}$ (the nematic phase).

At $T_{N-I}$, the nematic and isotropic phases can coexist, separated by a stationary interface. In our order-parameter model, this corresponds to $Q(y) = 0$ at $y = \infty$ and $Q(y) = Q_{N-I}$ at $y = -\infty$. In between, $Q(y)$ varies smoothly from 0 to $Q_{N-I}$, so that the interface has finite

width. In order to calculate the profile $Q(y)$, one solves the Euler-Lagrange equation associated with Eq. (A1), subject to the boundary conditions at $y = \pm \infty$. The resulting Euler-Lagrange equation from the minimization $\delta \gamma / \delta Q = 0$ gives

$$A \xi^2 \left[ \frac{\partial^2 Q}{\partial y^2} \right] = AQ - BQ^2 + CQ^3 , \tag{A5}$$

with solution

$$Q(y) = \tfrac{1}{2} Q_{N\text{-}I} \left[ 1 + \tanh \left[ \frac{-y}{2\xi} \right] \right] , \tag{A6}$$

where the actual (as opposed to bare) correlation length, is

$$\xi = \frac{1}{Q_{N\text{-}I}} \left[ \frac{2}{C} \right]^{1/2} , \tag{A7}$$

which gives a surface tension of

$$\gamma = \tfrac{1}{6} A \xi Q_{N\text{-}I}^2 . \tag{A8}$$

The latent heat of fusion per unit volume in this model is

$$\frac{L \rho_N}{M_w} = -T_{N\text{-}I} \left[ \frac{\partial F}{\partial T} \right]_{T_{N\text{-}I}} = \frac{a}{2} T_{N\text{-}I} Q_{N\text{-}I}^2 . \tag{A9}$$

The capillary length $d_0 = \gamma M_w / L \rho_N$ is thus given by

$$d_0 = \frac{1}{3} \xi \left[ \frac{T_{N\text{-}I} - T^*}{T_{N\text{-}I}} \right] = \frac{1}{3} \frac{\xi_0^2}{\xi} , \tag{A10}$$

where the correlation length is evaluated at $T_{N\text{-}I}$. One should note the above results imply that $\gamma \approx (T_{N\text{-}I} - T^*)^{3/2}$ whereas the latent heat vanishes linearly. Thus as Eq. (A10) shows, the ratio $\gamma / L$ also vanishes as $T_{N\text{-}I}$ goes to $T^*$, as the correlation length $\xi(T) = \xi_0 [(T - T^*)/T^*]^{-1/2}$ diverges. In terms of physical dimensions, we may understand the scaling in Eq. (A10) by noting that in this mean-field theory $A \propto 1/\xi^2$ and the order parameter $Q_{N\text{-}I} \propto 1/\xi$, so that

$$\gamma \propto \frac{1}{\xi^2} \xi \left[ \frac{1}{\xi} \right]^2 \propto \frac{1}{\xi^3} ,$$

$$L \propto \left[ \frac{1}{\xi} \right]^2 . \tag{A11}$$

Putting everything together we have $d_0 \propto 1/\xi$.

For 8CB, the physical correlation length[57] is measured to be $\xi = 70^{+70}_{-40}$ Å, and $T_{N\text{-}I} - T^*$ is measured to be $2.0 \pm 0.1\,°C$. Thus $d_0$ is predicted to be from 0.06 to 0.30 Å. From the measured values of $\gamma$ and $L$, we have $d_0 = 0.047 \pm 0.022$ Å. Given that we have neglected the effects of the tilt angle $\theta_t$, the agreement is satisfactory.

To summarize, the very small values of $d_0$ result from the weakness of the first-order transition. For a strongly first-order transition, $\xi \to \xi_0$ so that Eq. (A10) predicts that $d_0 \approx \xi_0$. In fact, typical solid-liquid transitions do have capillary lengths of a few angstroms.

*Present address: Laboratoire de Physique des Solides, Université de Paris–Sud, Bâtiment 510, 91405 Orsay CEDEX, France.

[1]Patrick Oswald, John Bechhoefer, and Albert Libchaber, Phys. Rev. Lett. 58, 2318 (1987).

[2]John Bechhoefer, Adam Simon, Albert Libchaber, and Patrick Oswald, in Random Fluctuations and Pattern Growth: Experiments and Models, edited by H. E. Stanley and N. Ostrowsky (Kluwer Academic, Dordrecht, 1988), pp. 93–100.

[3]J. S. Langer, Rev. Mod. Phys. 52, 1 (1980).

[4]D. Armitage and F. P. Price, Mol. Cryst. Liq. Cryst. 44, 33 (1978).

[5]Adam J. Simon, John Bechhoefer, and Albert Libchaber, Phys. Rev. Lett. 61, 2574 (1988).

[6]John Bechhoefer, Ph.D. thesis, University of Chicago, 1988.

[7]M. J. Aziz, J. Appl. Phys. 53, 1158 (1982).

[8]K. A. Jackson, G. H. Gilmer, and H. J. Leamy, in Laser and Electron Beam Processing of Materials, edited by C. W. White and P. S. Peercy (Academic, New York, 1980), p. 104.

[9]W. J. Boettinger, S. R. Coriell, and R. F. Sekerka, Mater. Sci. Eng. 65, 27 (1984).

[10]B. Caroli, C. Caroli, and B. Roulet, Acta Metall. 34, 1867 (1986).

[11]S. de Cheveigné, C. Guthmann, and M. M. Lebrun, J. Phys. (Paris) 47, 2095 (1986).

[12]B. Caroli, C. Caroli, and B. Roulet, J. Cryst. Growth 76, 31

(1986).

[13]L. D. Landau and E. M. Lifschitz, Statistical Physics, 3rd ed. (Pergamon, Oxford, 1980).

[14]D. J. Wollkind and L. A. Segel used the standard scaling in their amplitude-equation calculations but presented their results using a scaling very similar to the one adopted in this paper. See Philos. Mag. 268A, 351 (1970).

[15]W. A. Tiller, K. A. Jackson, J. W. Rutter, B. Chalmers, Acta. Metall. 1, 428 (1953).

[16]W. W. Mullins and R. F. Sekerka, J. Appl. Phys. 35, 444 (1964).

[17]A good summary of the principles of linear stability analysis may be found in S. Chandrasekhar, Hydrodynamic and Hydromagnetic Stability (Oxford University Press, Oxford, 1961), pp. 1–8.

[18]S. de Cheveigné et al., J. Cryst. Growth (to be published).

[19]W. J. Boettinger, D. Shechtman, R. J. Schaefer, and F. S. Biancaniello, Metall. Trans. 15A, 55 (1984).

[20]R. J. Schaefer, W. J. Boettinger, F. S. Biancaniello, and S. R. Coriell, in Laseres in Metallurgy, edited by K. Mukherjee and J. Mazumder (Metallurgical Society of AIME, New York, 1981), p. 43.

[21]A. Munitz, Metall. Trans. 16B, 149 (1985).

[22]For example, B. Caroli, C. Caroli, and B. Roulet, J. Phys. (Paris) 43, 1767 (1982).

[23]S. R. Coriell, G. B. McFadden, and R. F. Sekerka, Annu. Rev.

Mater. Sci. **15**, 119 (1985).

[24]J. D. Hunt, K. A. Jackson, and H. Brown, Rev. Sci. Instrum. **37**, 805 (1966).

[25]Hisao Esaki, Ph.D. thesis, Ecole Polytechnique Fédérale de Lausanne, Lausanne, Switzerland, 1986.

[26]H. Esaki and W. Kurz, J. Cryst. Growth **72**, 578 (1985).

[27]Mona A. Chopra, Ph.D. thesis, Rensselaer Polytechnic Institute, Troy, NY, 1983.

[28]William F. Kaukler, Ph.D. thesis, University of Toronto, Toronto, Canada, 1981.

[29]William F. Kaukler, Rev. Sci. Instrum. **55**, 1643 (1984).

[30]Mettler Instrument Corp., Highstown, NJ 08520 (Mettler Instrumente AG, CH-8606, Greifensee, Switzerland).

[31]BDH, Ltd., Broom Rd., Poole, BH12 4NN, England.

[32]International Products Corp., Trenton, NJ 08601.

[33]Fisher Scientific, Pittsburgh, PA 15219.

[34]Birendra Bahadur, Mol. Cryst. Liq. Cryst. **109**, 3 (1984).

[35]Frederic J. Kahn, Phys. Today **35**, 66 (1982).

[36]EM Industries, Inc., Hawthorne, NY 10532.

[37]Anotop 10 filter, Anotec Separations, Ltd. Banbury, Oxon, OX16 7RT England, distributed by Alltech Associates, Inc., Deerfield, IL 60015.

[38]Standard Safety Equipment Corp., Palatine, IL 60067. In the laminar-airflow hood, we use a glove box built in our laboratory.

[39]Glass Tek Industries, Morgan Hill, CA 95037.

[40]Devcon, Danvers, MA 01923.

[41]The Baker Company, Inc., Sanford, ME 04073.

[42]Omega Engineering, Inc., Stamford, CT 06907.

[43]Neslab Instruments, Inc., Newington, NH 03801.

[44]Newport Corp., Fountain Valley, CA 92708.

[45]Berger Lahr, D7630 Lahr, West Germany.

[46]Keithley Instruments, Inc., Cleveland, OH 44139.

[47]Olympus Corp., distributed by Scientific Supply Co., Schiller Park, IL 60176.

[48]Ealing Electro-Optics, Inc., South Natick, MA 01760.

[49]We wish to thank Peter Palffy-Muhoray at Kent State University for bringing this to our attention.

[50]Samir Ghodbane and Daniel E. Martire, J. Phys. Chem. **91**, 6410 (1987).

[51]H. Marynissen, J. Thoen, and W. Van Kael, Mol. Cryst. Liq. Cryst. **97**, 149 (1983).

[52]J. Frenkel, *Kinetic Theory of Liquids* (Clarendon, Oxford, 1946), pp. 200–208.

[53]*CRC Handbook of Chemistry and Physics,* edited by Robert C.

Weast, 64th ed. (CRC, Boca Raton, 1983), p. C-377. Compound No. 9196.

[54]H. Takezoe, M. Hara, S. Ichikawa, and A. Fukuda, Mol. Cryst. Liq. Cryst. **122**, 169 (1985).

[55]Michael E. Moseley and Aharon Loewenstein, Mol. Cryst. Liq. Cryst. **90**, 117 (1982).

[56]S. K. Ghosh and E. Tettamanti, Lett. Nuovo Cimento **40**, 197 (1984).

[57]S. Faetti and V. Palleschi, J. Chem. Phys. **81**, 6254 (1984).

[58]H. Yokoyama, S. Kobayashi, and H. Kamei, Mol. Cryst. Liq. Cryst. **129**, 109 (1985).

[59]D. Langevin and M. A. Bouchiat, Mol. Cryst. Liq. Cryst. **22**, 317 (1973).

[60]Richard Williams, Mol. Cryst. Liq. Cryst. **35**, 349 (1976).

[61]A. Béguin *et al.*, Mol. Cryst. Liq. Cryst. **115**, 119 (1984).

[62]B. R. Ratna and S. Chandrasekhar, Mol. Cryst. Liq. Cryst. **162B**, 157 (1988).

[63]D. Armitage and F. P. Price, Chem. Phys. Lett. **44**, 305 (1976).

[64]*Landolt-Börnstein Zahlenwerte und Funktionen aus Physik, Chemie, Astronomie, Geophysik, und Technik,* Band 2, Teil 8, edited by K. H. Hellwege (Springer, Berlin, 1962), pp. 5–565.

[65]Hai Perng Kuo and Seppo A. Korpela, Phys. Fluids **31**, 33 (1988).

[66]Boris I. Shraiman, Phys. Rev. A **36**, 261 (1987).

[67]J. P. Gollub and T. H. Solomon, in *Chaos and Related Nonlinear Phenomena: Where Do We Go From Here?,* Proceedings of the Fritz Haber International Symposium, 1986, edited by I. Procaccia (Plenum, New York, 1988).

[68]B. Caroli, C. Caroli, C. Misbah, and B. Roulet, J. Phys. (Paris) **46**, 401 (1985).

[69]P. G. de Gennes, Mol. Cryst. Liq. Cryst. **12**, 193 (1971).

[70]R. Lipowsky and G. Gompper, Phys. Rev. B **29**, 5213 (1984).

[71]Raymond E. Goldstein, Ph.D. thesis, Cornell University, 1988 (unpublished).

[72]H. J. Coles and C. Stratielle, Mol. Cryst. Liq. Cryst. **55**, 273 (1979).

[73]D. A. Dunmur and W. H. Miller, J. Phys. (Paris) C3, 141 (1979).

[74]N. V. Madhusudana and R. Pratibha, Mol. Cryst. Liq. Cryst. **89**, 249 (1982).

[75]A. G. Chmielewski, Mol. Cryst. Liq. Cryst. **132**, 339 (1986).

[76]Sandro Faetti and Vincenzo Palleschi, Phys. Rev. A **30**, 3241 (1984).

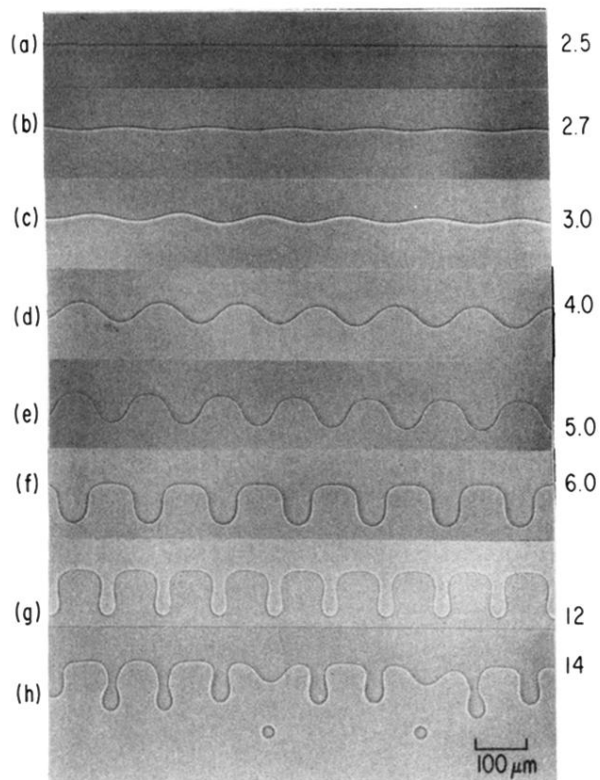[77]Eastman Kodak Co., Rochester, NY 14650. Catalog No. 102 3266.

FIG. 2. Interface patterns as the velocity is increased. The numbers to the right of each pattern give the velocity, in $\mu$m/sec. $G = 43\,°C/cm$, $c_0 = 3.0$ mol %, $d = 28\,\mu$m. Phase contrast illumination.